WPHCD-PR(17) 18844

C Wu et al.

Gyrotron Multistage Depressed Collector Based on ExB Drift Concept using Azimuthal Electric Field — Part I: Basic Design

Preprint of Paper to be submitted for publication in
Physics of Plasmas

This work has been carried out within the framework of the EUROfusion Consortium and has received funding from the Euratom research and training programme 2014-2018 under grant agreement No 633053. The views and opinions expressed herein do not necessarily reflect those of the European Commission.

Gyrotron Multistage Depressed Collector Based on $\boldsymbol{E}\times\boldsymbol{B}$ Drift Concept using Azimuthal Electric Field

Part I: Basic Design

Chuanren Wu (吴传人),[1] Ioannis Gr. Pagonakis,[1] Konstantinos A. Avramidis,[1] Gerd Gantenbein,[1] Stefan Illy,[1] Manfred Thumm,[1] and John Jelonnek[1]

Institute for Pulsed Power and Microwave Technology,

Karlsruhe Institute of Technology, Germany.

(Dated: November 17, 2017)

Multistage Depressed Collectors (MDCs) are widely used in vacuum tubes to regain energy from the depleted electron beam. However, the design of an MDC for gyrotrons, especially for those deployed in fusion experiments and future power plants, is not trivial. Since gyrotrons require relatively high magnetic field, its hollow annular electron beam is magnetically confined in the collector. In such a moderate magnetic field, the MDC concept based on $\boldsymbol{E}\times\boldsymbol{B}$ drift is very promising. Several concrete design approaches based on the $\boldsymbol{E}\times\boldsymbol{B}$ concept have been proposed. This paper presents a realizable design of a two-stage depressed collector based on the $\boldsymbol{E}\times\boldsymbol{B}$ concept. A collector efficiency of 77 % is achievable, which will be able to raise the total gyrotron efficiency from currently 50 % to more than 60 %. Secondary electrons reduce the efficiency only by 1 %. Moreover, this design is resilience to the change of beam current (i.e. space charge repulsion) and beam misalignment as well as magnetic field perturbations. Therefore, compared to other $\boldsymbol{E}\times\boldsymbol{B}$ conceptual designs, this design approach is simple, feasible and promising.

Keywords: Gyrotrons, Collectors, Drifts, ECRH

I. INTRODUCTION

Gyrotrons are microwave sources for electron cyclotron heating and current drive in fusion experiments. Like other vacuum tubes, in a fusion gyrotron electrons gain energy by an acceleration voltage, e.g. 80 kV in the ITER gyrotron[1]. Usually less than 35 % of the electron kinetic energy is converted to microwaves, thus still a large quote of the input electric energy remains in the spent electron beam. To partly recuperate this energy, depressed collectors have to be adopted in gyrotrons. Single-Stage Depressed Collectors (SDCs) being used in fusion gyrotrons[2–4] usually have 50 % to 60 % collector efficiency ($\eta_{\mathrm{col}} = P_{\mathrm{recovered}}/P_{\mathrm{spent\ beam}}$), which results in an overall gyrotron efficiency (η_{total}) of up to approximately 50 %. Even though, for a gyrotron with 1 MW or 2 MW output power, plenty of spent beam energy is converted to heat on the water-cooled collector. Taking other losses in a gyrotron into account, to accomplish the $\eta_{\mathrm{total}} > 60\,\%$ goal of efficiency, the collector efficiency should be $\eta_{\mathrm{col}} > 74\,\%$[5], which is beyond the capability of a SDC. In order to achieve this goal, the depressed collector should be extended to multiple stages, so called Multistage Depressed Collector (MDC).

MDCs have been widely applied in other vacuum tubes, especially in the traveling wave tubes where high efficiency is demanded[6,7]. However, to the best knowledge of the authors, no experiment on MDC for gyrotrons has been published yet. There are several reasons, which cause the design of a gyrotron MDC non-trivial. Firstly, there is still a strong magnetic field in the gyrotron collector region, which is above 100 mT at collector entrance. The field remains at tens of mT even after 1 m axial offset in the collector. Sorting electrons in such a twisted electron beam confined by magnetic field is difficult. Moreover, the impacting area on electrodes is limited by the bundle of the electron beam, which is determined by the magnetic confinement. The straightforward solution targeting the magnetic field is to weaken it until approximately 10 mT. Within the weak magnetic field, the electron beam will be slightly confined. If the demagnetization takes place inside a short distance, such that the transition is nonadiabatic, then the electrons may be energy-sorted and spread in a wide area[8–10]. Secondly, fusion gyrotrons have annular electron beams with small orbits. If the electric and magnetic scalar potentials are axisymmetric, the magnetic flux enclosed in the electron beam is constant (Busch theorem). In order to increase the thickness of the electron beam without increasing the collector size a lot, the cross section of this flux should not

expand. For this reason, additional coils or ferromagnetic poles are usually inserted near the axis in the nonadiabatic approach[5,8,9]. Thirdly, in existence of the magnetic field, secondary electrons (including the elastically and inelastically reflected ones) can follow the magnetic field lines, forms a current between stages, which reduce the efficiency and can even move back beyond the entrance of the collector.

Beside the conventional nonadiabatic approach described above, another gyrotron MDC concept based on the $\boldsymbol{E}\times\boldsymbol{B}$ drift has been proposed[11]. This concept makes use of the $\boldsymbol{E}\times\boldsymbol{B}$ drift to perfectly sort and distribute electrons, while the same drift also prevent the secondary electrons being returned. Therefore, this concept seems to be very promising. Three kinds of MDC design approaches based on the $\boldsymbol{E}\times\boldsymbol{B}$ concept have been proposed[12], where the drift can be planar or radial, depending on the orientation of the fields. For the planar drift case, the hollow annular electron beam is transformed firstly into one or more sheet beams. Then the $\boldsymbol{E}\times\boldsymbol{B}$ drift is applied on the sheet beams[13,14]. In the radial drift approaches, there will always be a longitudinal component of the electric field to decelerate the electrons and also a longitudinal component of the magnetic field retained from the gyrotron magnet. Beside these field components, in order to create a radial drift, an azimuthal electric field can be applied using electrodes in helical shapes[11,15]; alternatively, the azimuthal component of the magnetic field induced by a special type of collector coils can also create the radial drift[16].

Among the various MDC designs, the azimuthal electric field approach[15] requires just a simple magnetic system and therefore may be easy to realize. In this paper, the design details of this approach and its simulation results will be given in Section II and III, respectively. Afterwards, the tolerance of this design will be investigated in Section IV.

II. BASIC DESIGN

A. Principle

The essential part of this design approach is to create a radial electron drift. In this particular case, an azimuthal electric field component serves the creation of that drift, as shown in Fig. 1. Generally, stronger drift implies larger drift distance D (marked in Fig. 2 and Fig. 6). A large drift distance is preferred for a clean sorting of electron kinetic energy, such that the high-energetic fraction of the electron beam will not be very close to the

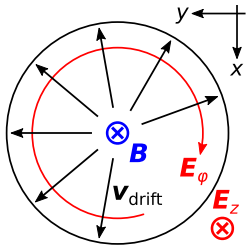

FIG. 1: Sketch of the field components and electron drift velocity

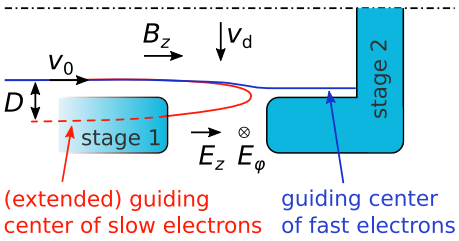

FIG. 2: Principle of the $\boldsymbol{E}\times\boldsymbol{B}$ concept

less-depressed electrodes and get collected accidentally where they are not expected to be. Besides, a large drift distance also relaxes the precision requirement of the magnetic field and improves the tolerance. As the drift velocity

$$\boldsymbol{v}_d = \frac{\boldsymbol{E}\times\boldsymbol{B}}{B^2} \tag{1}$$

and the drift distance D is inversely proportional to the magnitude of the magnetic field[14], for a low-frequency gyrotron like a 28 GHz industrial gyrotron[17], where the magnetic field is weak, only a small size is required for such an $\boldsymbol{E}\times\boldsymbol{B}$ MDC to obtain enough drift. In that case, the magnetic field in the collector can be kept homogeneous (pure axial) like in Fig. 1, which would be a primitive model. However, for high-frequency fusion gyrotrons, to sustain a homogeneous magnetic field in the collector region is unpractical. Therefore, the diverging flux from the gyrotron magnet is slightly tuned in the collector region, instead of creating an artificial homogeneous field. An adjusted Single-Stage Depressed Collector (SDC) for the ITER 170 GHz gyrotron[1] with tuned magnetic field is taken as the starting point. Fig. 3 shows the contour of this SDC. The most important part is the red marked "slope" segment on the collector wall, where the magnetic field is aligned locally. Since the electron trajectories follow magnetic field lines in the absence of drifts, the guiding centers of electrons are parallel to the slope. The electron beam keeps several centimeters off the collector wall because of these configurations.

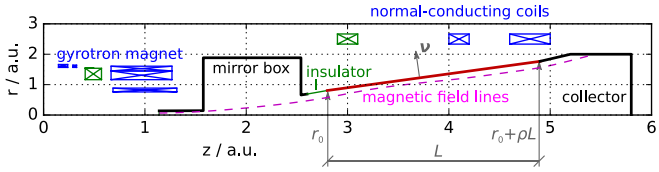

FIG. 3: Contour of a SDC model as the base for the MDC

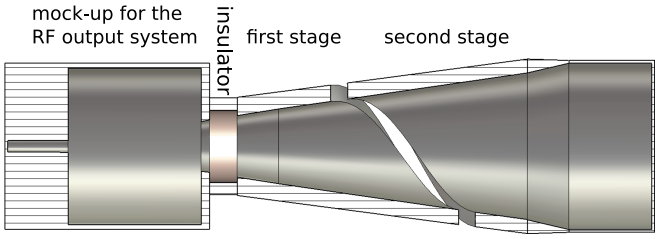

(a) cut view

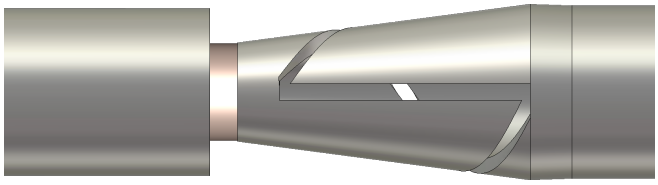

(b) full view

FIG. 4: Geometry of the new two-stage collector

Starting from this SDC, a two-stage depressed collector based on the $\boldsymbol{E}\times\boldsymbol{B}$ drift will be conceptually designed. To minimize the details of the CAD model, the wall of the SDC is represented by a thick metallic layer. Distinct from the multiple electrodes in the similar design[11], this paper proposes one single-turn helical slot on the collector wall, which separates the electrodes and introduces an azimuthal electric field component. The torsion of this helix determines the drift strength.

The simplified CAD model is shown in Fig. 4. Depending on the properties of the spent electron beam, different depression voltages are applied on each stage. In this example, $-30\,\mathrm{kV}$ and $-42\,\mathrm{kV}$ depression are chosen, while the kinetic energy of the spent electrons varies from $38\,\mathrm{keV}$ to $130\,\mathrm{keV}$. Slow electrons up to $42\,\mathrm{keV}$ and reflected secondary electrons will be steered by the drift that they will impinge the helical cut surface of the first electrode, whereas the fast electrons will travel further and reach the final cylinder bulk, as presented by Fig. 10 in Section III. A local axial sweeping of the electron beam on the cylinder is possible.

There is a straight slot joining the both ends of the helix for simplicity, shown in Fig. 4b. This structure causes an opposite drift, which may reflect a tiny fraction of electrons. The reflection of electrons could be minimized or even conceptually avoided, however in the price of increasing the complexity. Part II of this work will propose some improved designs, which will minimize the reflected current.

B. Modeling

Except the technical limitations on the minimum achievable collector size (such as thermal loading or other technological issues), there is a more fundamental theoretical constraint, from which the minimum size of the collector can be derived. Based on this analysis, the working point is chosen.

The goal is to determine the $\boldsymbol{E}\times\boldsymbol{B}$ drift distance D along the helix, which according to the previous work[14] is

$$D = \frac{2\,v_0\,m_0}{B\,q}\,\tan\phi = \frac{2\,v_0\,m_0}{B\,q}\,\frac{\sqrt{1-\cos^2\phi}}{\cos\phi}\;, \tag{2}$$

where ϕ is the angle between electric and magnetic field. Eq. (2) also shows that, the drift distance is independent of the magnitude of the electric field in this model. The analysis can be subdivided into four steps: in the first step, a mathematical description of the helix will be given; the second step is an approximate description of the magnetic field and the third step is the calculation of the angle between fields; finally, all variables will be substituted into (2).

Firstly, the function of a helix curve $\boldsymbol{h}$ starting from $z = z_0$ and going to $z = z_0 + L$ has the form

$$\boldsymbol{h}(z) = (h_x, h_y, z - z_0)\;, \tag{3}$$

which should be mathematically simple for any CAD description and will hopefully also be beneficial for the later construction, even if this simple kind of helix could be neither optimal for efficiency nor for size. With the variable of relative axial displacement

$$l := z - z_0\;, \tag{4}$$

in range $l \in [0, L]$, one can define the radius r and phase φ of the helix on a conical surface as

$$r = r_0 + \rho\,l\;, \tag{5a}$$

$$\varphi = 2\pi \frac{l}{L} \,, \tag{5b}$$

where L is the axial height of the helix, r_0 is the initial radius and $\rho \geq 0$ as marked in Fig. 3. Transforming $\boldsymbol{h}$ in Cartesian coordinates yields

$$h_x = r\cos\varphi = (r_0 + \rho\, l)\cos 2\pi \frac{l}{L} \,, \tag{6a}$$

$$h_y = r\sin\varphi = (r_0 + \rho\, l)\sin 2\pi \frac{l}{L} \,. \tag{6b}$$

Accordingly, the growing direction of the helix is

$$\boldsymbol{h}' = \frac{\mathrm{d}\boldsymbol{h}}{\mathrm{d}l} = \left(\frac{\mathrm{d}h_x}{\mathrm{d}l}, \frac{\mathrm{d}h_y}{\mathrm{d}l}, 1 \right) \,. \tag{7}$$

Another auxiliary vector is the normal vector of the conical surface, where the helix is located. It has the direction

$$\boldsymbol{\nu} = (\cos\varphi, \sin\varphi, -\rho) \,, \tag{8}$$

which is also marked in Fig. 3.

Secondly, since the local magnetic field is approximately parallel to the conical surface and free of any azimuthal component (see Fig. 3), the expressions for the components of the magnetic flux density on the cone are

$$B_z = |B| \, \frac{1}{\sqrt{1+\rho^2}} \,, \tag{9a}$$

$$B_r = |B| \, \frac{\rho}{\sqrt{1+\rho^2}} = \rho\, B_z \,. \tag{9b}$$

For the calculation of $|B|$ it is reasonable to assume that the B_z would be nearly constant over r ($\pm 2\,\%$ error in this example). According to the flux conservation,

$$B_z = \frac{\psi}{\pi\, r^2} \,, \tag{10}$$

where ψ is the magnetic flux enclosed by a circle with radius r, the magnetic flux density on the wall is

$$\boldsymbol{B} = \frac{\psi}{\pi\, r^2} \, (\rho\cos\varphi, \rho\sin\varphi, 1)^{\mathrm{T}} \,. \tag{11}$$

Thirdly, in order to calculate the angle ϕ, the direction of the local electric field is required. Suppose there is a vector $\boldsymbol{\mathcal{E}}$ aligned with the $\boldsymbol{E}$ field inside the helical cut, i.e.,

$$\boldsymbol{\mathcal{E}} = a\, \boldsymbol{E} \,, \tag{12}$$

for $a \in \mathbb{R}^+$. The electric field has to fulfill three conditions:

1. $\boldsymbol{\mathcal{E}}$ is tangential to the surface of the cone, where the helix is located

$$\boldsymbol{\nu} \cdot \boldsymbol{\mathcal{E}} = 0 \; . \tag{13a}$$

2. $\boldsymbol{\mathcal{E}}$ is perpendicular to the helical electrode surface on the first stage, where the electrons will be collected, i.e., perpendicular to the growing direction of the helix

$$\boldsymbol{h}' \cdot \boldsymbol{\mathcal{E}} = 0 \; . \tag{13b}$$

3. $\boldsymbol{\mathcal{E}}$ points towards the second stage

$$\mathcal{E}_z > 0 \; . \tag{13c}$$

One solution to these three criteria is

$$\boldsymbol{\mathcal{E}} = \begin{pmatrix} 2\pi r\rho\cos\varphi + L(1+\rho^2)\sin\varphi \\ 2\pi r\rho\sin\varphi - L(1+\rho^2)\cos\varphi \\ 2\pi r \end{pmatrix} \; . \tag{14}$$

Finally, the scalar production of (11) and (14) gives the angle between electric and magnetic field

$$\cos\phi = \frac{\boldsymbol{\mathcal{E}} \cdot \boldsymbol{B}}{|\mathcal{E}|\,|B|} \; . \tag{15}$$

The drift distance D is calculated by substituting (11) and (15) into (2), which leads to a very lengthy equation. The elegance of this model is that this lengthy drift distance equation has an equivalent simple form:

$$D = \quad \frac{m_0\, v_0\, L}{q\, \psi}\, r \quad = \quad \frac{m_0\, v_0\, L}{q\, \psi}\, l + \frac{m_0\, v_0\, L\, r_0}{q\, \psi} \; . \tag{16}$$

Eq. (16) means that the $\boldsymbol{E}\times\boldsymbol{B}$ drift distance increases linearly with the longitudinal offset l of a point on the helix.

Considering the space charge effect and the retarding voltage on the first collector stage, after an electron passes through the first stage into the $\boldsymbol{E}\times\boldsymbol{B}$ region, its velocity v_0 has the minimum value corresponding to 12 keV, according to the simulation. Inserting the minimum of v_0 into (16), the minimum of the drift distance is obtained. Figure 5 shows the relation of minimum drift distance with electrode radius and collector length.

In principle, the minimum drift distance is preferred to be large. However, a large distance demands low magnetic field or large angle between the fields, which correspond to large radius and long collector geometry, respectively according to (16).

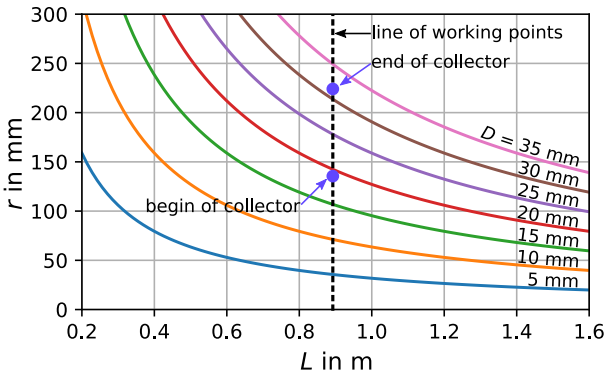

FIG. 5: Minimum drift distance related to radius and collector length

On the practical side, in order to keep the length of the MDC comparable to a SDC, the length (height) of the cone is fixed at $L = 0.9\,\mathrm{m}$ and the maximum radius of the helix shall be below 225 mm. This configuration results in a drift distance of around 2 cm at the beginning of the helix and above 3 cm at its end. This is the maximum allowed distance between the electron beam and the conical wall, which is controlled by the local magnetic field and indirectly tuned by the current of the auxiliary coils.

III. SIMULATION

There are two methods available to simulate MDC models, namely trajectory TRacKing (TRK) and the Particle-In-Cell (PIC). At the time of writing this paper, just few simulation software can deal with both methods on such three-dimensional irregular models. For the simulation of this particular MDC model, CST Particle Studio is used, where the PIC method implemented in CST does the full electromagnetic wave simulation, rather than only electrostatic. Copper with the Furman model for the secondary emission has been built in CST and therefore used in the simulations. It takes the elastic reflections also into account.

However, even with recent computational resources it is still not trivial to simulate this MDC. Firstly, unlike the MDC of an X-band gyro-backward-wave oscillator with lower magnetic field[18], the 170 GHz ITER gyrotron considered in this model has 6.77 T magnetic field in the cavity, therefore the magnetic field the collector is strong. If the magnetic field is too strong, the $\boldsymbol{E}\times\boldsymbol{B}$ drift will not be effective, as shown by (2). In order to reduce the strong magnetic field within a usable range, a huge volume is required to dilute the field. As a consequence of the huge 3D simulation volume, the number of required mesh cells is too large

for a normal PC in both simulation methods. Secondly, the injected electron beam has to be presented with a large number of (macro) sampling electrons, in order to statistically resolve the azimuthal properties of the electron beam. In addition, the facts that the simulation volume is large and electrons are decelerated, it takes a long simulation time (many steps) until any (especially a low-energetic) electron travels through the whole MDC length and is collected. With a transient method like PIC, this also means that plenty of injected electrons are within the simulation volume at the same moment. So that the particle-pushing process can be resource hungry. Thirdly, when an electron impacts the electrode, secondary electrons (including the elastic, inelastic and the low-energetic true secondary electrons) are emitted from that surface, where the emitted current can even be higher than the impacting one. It will bring additional electrons into the simulation volume and slow down the particle pushing significantly. Depending on the software implementation of the secondary electron model, a large number of electrons has to be injected, to get a statistically good sampling of secondary electrons in this 3D MDC model.

Therefore, a compromise has to be made between the computational resources and the accuracy. As it will be shown later, the sampling density of the injected electron beam seems to have more influence on the result quality than the other factors. Also storing beam electrons consumes the most of memory in both methods. With the available commercial software and resources, the expected phenomena of this MDC can be observed in the simulation using limited mesh densities and convergence can be obtained. The results of TRK and PIC methods are in close agreement with each other.

A. Trajectory (TRK) simulation

With the TRK method, the trajectories of electrons are simulated in multiple iterations. The change of the electric potential or charge (depending on the solver) between two iterations are recorded to consider space charges. In this way, the system may evolve to a steady-state.

Figure 6 is a cross section of the electron beam in the middle of the MDC, simulated with the TRK method. All electrons with kinetic energy higher than 10 keV are shown in red for a better demonstration. The figure shows the steady-state, rather than a transient moment, which means that all electron spots shown in this diagram belong to the same cut-plane but probably at different temporal moment. It can happen that one electron

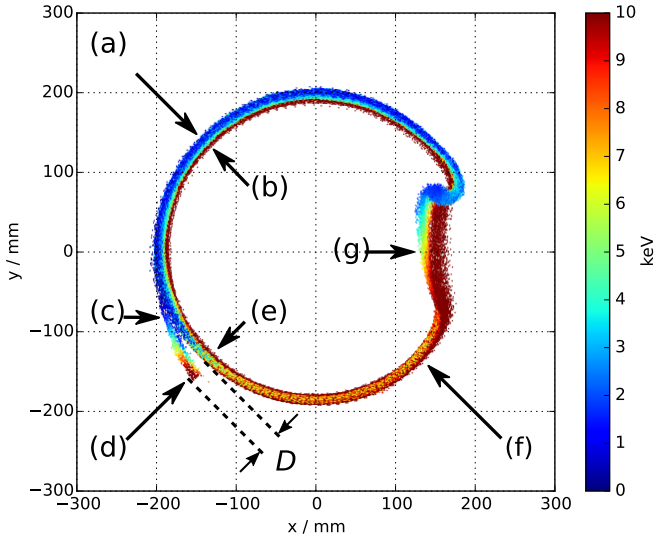

FIG. 6: Cross section of the electron beam in steady-state simulation

appearing at this diagram several times, because it may be decelerated later and passes through this cut-plane more than one time. Even though a small fraction of electrons may be back-and-forth reflected (will be described in the next paragraphs) no electron should be trapped and the simulation of a space-charge iteration stops only when all electrons are collected.

In Fig. 6, (a) and (b) are the electrons, which have already passed through the gap between the stages. They have lost kinetic energy. The outer side (a) are the slower electrons, whereas the faster electrons are on the inner side (b) because the slower electrons stayed longer in the radial drift region and hence, they had enough time to drift further (this should not be mixed with (2), where every electron was assumed to be totally decelerated). The electrons, which will be collected on the first stage, are firstly decelerated and then accelerated during their drifting towards the helix electrode (see also the white trajectory in Fig. 7). Electrons pointed by (c) in Fig. 6 are under deceleration and (d) are the ones, which are being again accelerated. Since this diagram is a cross section in the case of steady-state and the drift direction is radial, the electrons pointed by (d) are the same as those under (e). (f) are the electrons, which have not entered the helical gap yet. Those electrons pointed by (g) are at the specific angle where the drift has opposite direction. They will not be optimally collected and will be discussed in the next paragraphs.

Figure 7 shows some representative electron trajectories and the steady-state of the electric potential in the simulation region, while taking space charges of both primary and

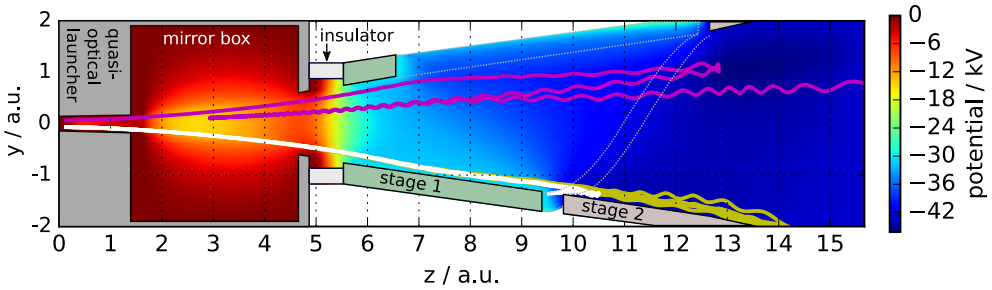

FIG. 7: Electrical potential considering space charge (including that of secondary electrons) in z-y-plane and some representative electron trajectories

secondary electrons into account. A typical low-energetic electron has the white trajectory. It is collected on the helical surface; whereas the yellow ones are the high-energetic electrons, which are collected on the second stage, as expected. The magenta trajectory represent one of the electrons, which are on the specific azimuthal angle. At this angle the ends of the helix are separated by a straight slot, thus the drift is in the opposite direction. In this particular example, the magenta electron at this angle encounters an undesired drift towards the center and does not have enough longitudinal velocity to land on the second stage, therefore it turns back to the mirror box with enlarged cyclotron motion. This kind of reflected electrons has only a small chance to pass through the mirror box because of the nonreciprocal increment of cyclotron motion, more probably it will turn back and enter the MDC again with a different azimuthal angle. The change of angle is the consequence of azimuthal drifts. At another angle, some of these electrons overcome the potential barrier caused by the retarding voltage and the asymmetric space charge. These electrons will be collected either on the second stage like in this example or on the first stage.

Although this concept-approval basic design is simple and promising, it is not perfect. There will be electrons escaping from this mechanism and they will return to the quasi-optical launcher or even travel backwards into the cavity. However, the reflected electrons are just a tiny fraction of the whole electron beam. The reasons for this are:

1. The electrons at this special angle are only a small part of the injected spent electrons.

2. Among these electrons, only the low-energetic ones are probably reflected by the retarding voltage.

3. From these reflected low-energetic electrons, some turn back and forth for one or

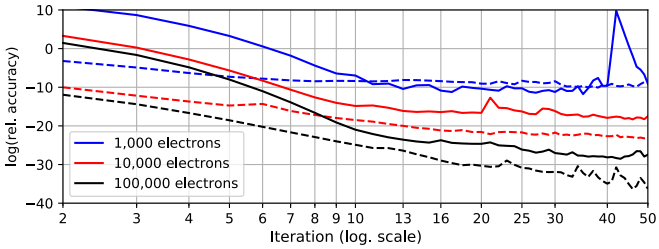

FIG. 8: Relative TRK iteration accuracy, solid lines take secondary electrons into account, while dashed lines not

multiple times and are finally collected by an electrode at another azimuthal angle. Only a small portion of them can reach the launcher (any electron that reaches the launcher is considered to be lost in the later calculation of collector efficiency)

4. The back-streamed electrons may or may not influence the interaction. This has to be further investigated. In addition, in the experiment with SDCs, the measured body current is far less than the lost current of secondary electrons predicted by the simulation.

Therefore, the finally reflected electrons are just a small portion of a small portion from the electrons at this specific azimuthal angle. In this (not optimized) simulation example, the reflected electron beam has 1.5 % current of the injected one (700 mA of totally 45 A), considering secondary electrons. Optimizations like reducing the width of the straight slot and increasing the drift distance on the helical part will reduce the reflected current, but this issue shall nonetheless be solved fundamentally.

The sampling of electrons influences the convergence of TRK iterations the most. Figure 8 shows the accuracy convergence of the TRK solver over iterations. The logarithmic accuracy is defined as

$$\delta_{\mathrm{dB}} = 20 \log_{10} \frac{|\boldsymbol{q}_{i+1} - \boldsymbol{q}_i|}{|\boldsymbol{q}_{i+1}|} \tag{17}$$

in CST, where $\boldsymbol{q}_n$ is the charge distribution in the n-th iteration. The noise level in the TRK convergence is the combined results mainly from two aspects:

- The small fraction of reflected electrons by the opposite drift may cause changes of space charges in each iteration, unless there is a dense sampling of electrons at the specific angle to present the space charge statistically accurate.

- Secondary electrons are numerically hard to sample within limited computational resources. The common model for the secondary emission has to limit the number and generation of secondary electrons, so that a few secondary electrons are emitted at random angles with random initial energy have to delegate the "cloud" of secondary electrons in the real world. The randomness brings extra noise.

Three pairs of simulations having the same design and mesh are compared as examples. Each pair contains the realistic simulation (solid line) and the variant without secondary electron (dashed line) as a reference simulation. In this way, the contributions of the two kinds of noise sources can be distinguished.

The only difference between the pairs of simulation setup is the number of injected electrons. Generally, the more number of electron samples the electron beam have, the less will be the noise. After several iterations, the decrement of the charge difference slows down. The distances between the dashed lines show about 10 dB convergence improvement per 10 times of the number of electrons, because there are more samples of the electrons under the opposite drift direction. If the distributions of these electrons are well resolved (the 10 k and 100 k cases), the randomness of secondary electrons adds another 5 dB to the convergence noise.

The TRK solver shows a collector efficiency of $\eta_{\mathrm{col}} = 79\,\%$ in absence of secondary electrons and 78 % if taking secondary electrons into account. This collector efficiency should be sufficient to raise the overall gyrotron efficiency above 60 %.

B. Verification with full-wave Particle-In-Cell (PIC)

In order to verify the steady-state TRK results, this MDC model is cross-checked with full-wave PIC simulations, which are more time and memory consuming than the TRK method. Although the PIC simulation is transient, after several hundreds of nanoseconds, the system may reach a steady state, but with a lot of noise. Like the observation in the TRK simulations, noise is mainly introduced by the statistical sampling of the primary and secondary electrons.

Figure 9 shows an example of the PIC convergence compared with the TRK result. The impacted current in this diagram consists of the primary electron beam as well as the multiple times collected secondary electrons. The same MDC model is investigated

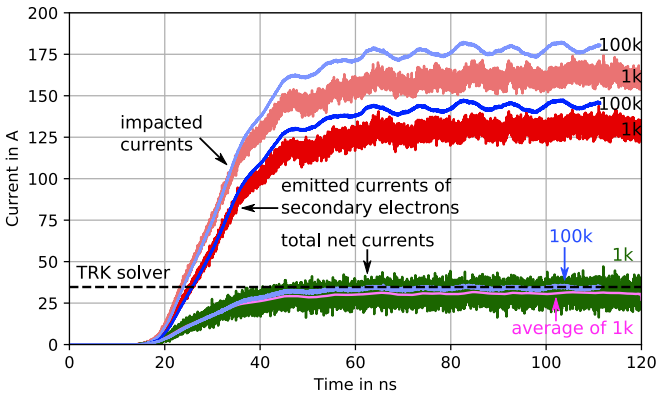

FIG. 9: PIC convergence related to the number of electrons, taking the current on second stage as example

within two simulations. The quantity of injected electrons at each time step is the difference between both simulations. In the first simulation, one thousand electrons are injected at each time step (marked by 1 k in Fig. 9). These electrons are distributed quasi-homogeneously around the azimuthal angle. In the second simulation, the same electron beam is sampled with 100,000 macro electrons each time step, while keeping the total charge and current unchanged (marked by 100 k in Fig. 9). Since the latter electron beam has a better statistical representation of the beam electrons, the noise observed in the simulation is many magnitudes lower. In addition, the more primary electrons impacting the electrode, the larger total number of secondary electrons is considered by the implementation in CST, i.e., larger number of electrons will represent the secondary electron yield more accurately. For this reason, both impacted and emitted current of the 100 k configuration are higher than in the 1 k case. In spite of the difference in the absolute values, both configurations have their (average) net current ($I_{\mathrm{impact}} - I_{\mathrm{emit}}$) at the same level, even though in the 1 k case the current simulation is more noisy.

Because the spent electron beam of gyrotrons has a broad energy spectrum and is injected from the launcher, a fast electron in the beam may need only tens of nanoseconds to travel through the entire collector region up to the second stage; while at this moment, the slow electrons may not yet pass the mirror box. For this reason, the transient current on the second collector stage evolves faster into a steady state than on the other parts of the MDC. Since the simulation with 100 k new electrons per step in such huge geometry is very time consuming (which would take months for hundreds of nanoseconds), it has to stop at 110 ns

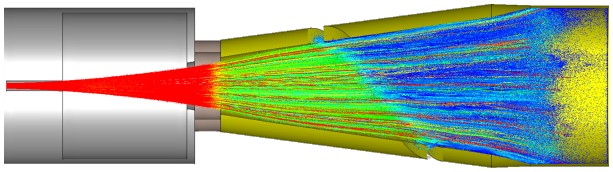

FIG. 10: Electron positions (including secondary electrons) in an arbitrary transient time step of PIC simulation

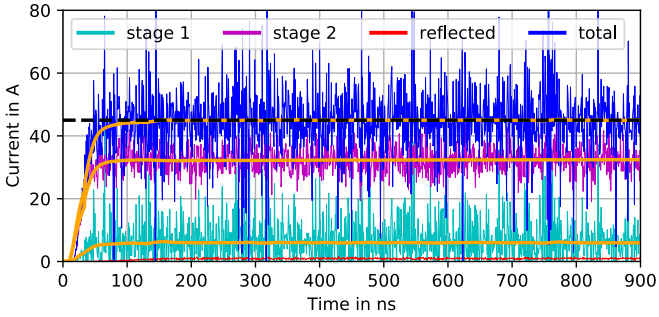

FIG. 11: Transient currents from the PIC simulation, their average values (orange), and the desired total current (dashed)

limited by the computational resources. Fortunately, this duration is already enough to drive the current on the second stage into a steady state, as shown in Fig. 9. To compare the net current in both cases, the average value for the 1 k case is calculated. In the steady state, the average current is not far away from the TRK simulation result, whereas with a denser sampled electron beam (i.e. the 100 k case), the current predicted by the PIC and TRK methods are in close agreement.

Considering the limitation of the computational resources, the presentation of the PIC simulation in the following paragraphs will focus on the 1 k per step case, which is not perfect, but its average value is also roughly in agreement with the TRK result.

Figure 10 shows a snapshot of the electron position in a hollow beam during the PIC simulation, which is in the same view as Fig. 4a. The colors of electrons stand for their kinetic energy, with red for high energy and blue for low energy. The whole electron beam is decelerated by 30 kV immediately after it enters the collector. Then the helical electrode splits the low-energetic electrons out. The sparse electrons appear on the end of the second stage are mostly the slow-moving secondary electrons.

In Fig. 11 all net currents are shown from a PIC simulation, which takes secondary electrons into account. The orange lines are the average value of each noisy curve. As

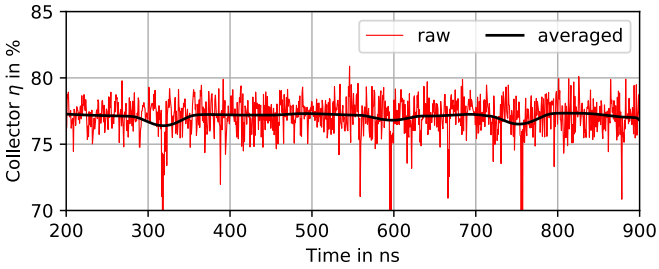

FIG. 12: Collector efficiency considering secondary electrons

expected, the average current on the second stage stabilized inside the first 100 ns, whereas the whole system evolves into a steady state 50 ns later, due to the slow electrons. The average value of the total collected current in the steady state is in perfect agreement with the expected 45 A injected current (dashed line), this means that no electron is trapped.

Finally, the efficiency of the collector is shown in Fig. 12. A collector efficiency of 77 % in average is observed in the PIC simulation, which considers the effects of secondary electrons; whereas in absence of secondary electrons, the MDC performs only 1 % better. This means that this kind of MDC handles secondary electrons well. The predicted efficiency by PIC simulation is in agreement with the TRK result.

C. Thermal loading

On the second stage, the decelerated electron beam can be axially swept, moreover, cooling a cylindrical surface might be easier than cooling the first stage, which is on a helical surface with gradually increased radius. Therefore, more attention has been paid on the cooling demand of the first stage. However, obtaining the thermal loading of such irregular 3D surface can be tricky for the currently available simulation tools.

Due to the limitation of the software implementation at the time of writing this paper, the thermal loading is calculated by CST in power per volume. However, it makes more sense to obtain the local value of the collected beam power per area, which has not been implemented in CST yet. Neither is the analysis of exported particle trajectories an option, because the lacking of internal information from the commercial software. After all, since the collected power on any object is obtainable, a work around would be overlaying a thin layer above the helical surface of the electrode. This thin layer consists of plenty of small mesh fragments, each of which is an individual object. The collected power of each fragment

can be obtained from a simulation and the area of its surface is known, thus the power per local area information is calculable. This method only provides quite rough information, but at least it is now capable to estimate an approximation of the thermal loading.

To plot the thermal loading of the curved helical electrode surface in a figure, the surface is projected in the transversal plane, which maps the mesh fragments to sectors. The power density is treated as a constant over each fragment. Figure 13 shows the distribution of power density on the sectors. The power is concentrated just on the inner edge of the helical surface, and there is no leakage of current observed in the simulation. This means that the choice of the helix thickness is conservative and the electrode can be narrower and compacter than in this example. The transition of colors was expected to be more gradually, probably because of the noise mentioned in the previous sections (which is hard to proof under the current resource and software implementation), the level of power density between two adjacent fragments can be sometimes quite different, and the noise may cause some hot spot in the region with high loading. Most fragments have thermal loading below $400\,\mathrm{W/cm^2}$ in the steady state. The region near the entrance of the collector (negative x in the diagram) has somewhat higher loading than the region near the end of the collector. The reason is that at the entrance of the collector, the helix has smaller radius than at the end; in addition, the electron beam is also more focused at the entrance. Hence, the density of impacting electrons is higher at the entrance and thus the thermal loading is also higher there. If the area of a fragment is tiny, even a single impacted (macro) electron would cause significant power density. As in this diagram, each fragment is radially less than 3 mm wide. The oddly high loading will vanish, if the "hot" fragments are averaged with the neighboring ones, becoming 6 mm fragments. Therefore, it is tricky to present the surface power density statistically accurate. The torsion of the helix could be tuned to achieve a homogeneous thermal loading profile. Nevertheless, due to the capability of the available simulation software, no further optimization step has been taken regarding the thermal loading.

IV. TOLERANCE

$\boldsymbol{E}\times\boldsymbol{B}$ drift sorts electrons reliably, since the sorting depends on the electric potential of the stages, rather than the local electric field. The sorting relies neither on the space charge repulsion nor the divergence of the magnetic flux. Besides, the moderate magnetic field

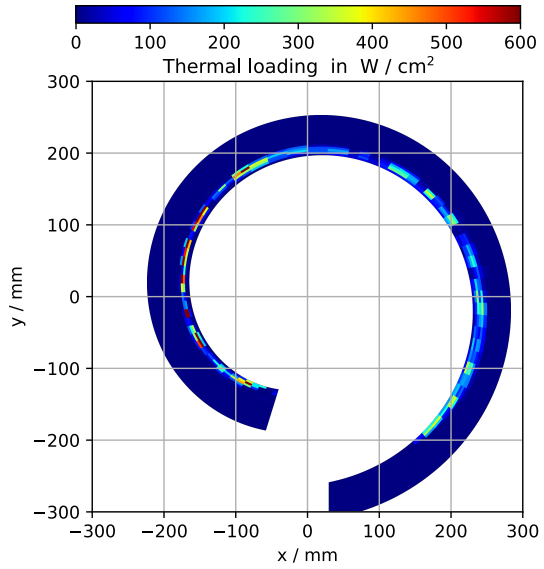

FIG. 13: Thermal loading on the surface of the first collector stage

inside the collector still confines and stabilizes the electron beam (in this example: 60 mT at the entrance, while 15 mT at the end). Therefore, this sorting mechanism should be stable to the variation of beam current (space charge) and does not require the magnetic field to be highly precise at low magnitude, the latter one also means that this kind of MDC may tolerate undesired perturbation of the magnetic field. In this section, the performance of this MDC will be investigated, in particular on three effects:

1. influence of the beam current, which is related to the space charge and repulsion;

2. undesired magnetic field perturbations, which come from the stray fields of the fusion tokamak and neighboring gyrotrons;

3. misalignment of electron beam;

which may influence the performance of a conventional gyrotron MDC.

To investigate the MDC performance regarding a variable beam current, simulation have been performed with only the beam current being scaled in a range of ±20 %, while keeping the kinetic energy spectrum of the electron beam and the retarding voltages of the MDC unchanged. Figure 14 presents the collected power over the beam current from the simulations, considering repulsion as well as induced electrical potential energy by the space charges. The collected beam power follows the beam current linearly. Moreover, the ratio

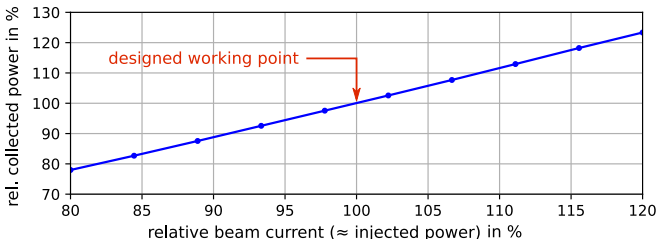

FIG. 14: Influence of beam current on the collected power

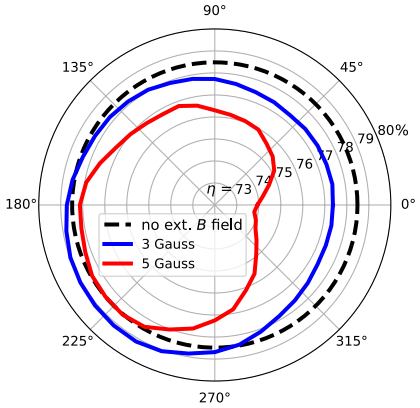

FIG. 15: Collector efficiency in an external magnetic field

between both is almost unity, which means that the performance of this MDC does not rely on the beam current.

From tokamak and neighboring gyrotrons there could be stray magnetic field, which may influence the performance of a single or multi-stage depressed collector. As presented in the literature[19,20], 5 Gauss would be a reasonable example for the stray magnetic field from the environment. Based on the simulation in Section III, an additional homogeneous transversal magnetic field with variable azimuthal angle is applied in the entire collector region. Figure 15 shows the efficiency of this MDC in an external perturbation magnetic field, where the direct path connecting the ends of the helix is located at 0°. In order to keep the time duration for the simulations acceptable, secondary electrons are not considered. Since the MDC geometry and its electric field is not axisymmetric, the resulting efficiency diagram is also excepted to be anisotropic. In the worst case of this example, the two-stage collector still has 73 % collector efficiency under a 5 Gauss transversal stray magnetic field, which nearly accomplishes the desired value of 74 % for the goal $\eta_{\text{total}} > 60\,\%$. If the collector could be positioned in the magnetic field with the optimum orientation, its efficiency would not be influenced by the external magnetic field.

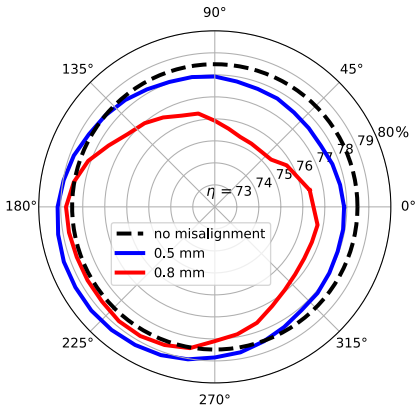

FIG. 16: Collector efficiency with misaligned electron beam in the cavity

The electron beam could be up to 0.5 mm misaligned in cavity still allowing single-mode oscillation[21]. A realistic MDC should be capable of tolerating this misalignment. The tolerance is again checked by simulations, where only the injecting position of the electron beam should be shifted, while keeping the magnetic field and the geometry always centered. Even though this method is not strictly correct (a misaligned electron beam would have slightly different energy and pitch factor distributions), it is acceptable for the demonstration. Because in the collector simulation the electron beam is injected from the launcher, the beam misalignment in the cavity is approximately converted to the one in the injection position via

$$\Delta r_{\mathrm{inj}} = \sqrt{\frac{B_{\mathrm{inj}}}{B_{\mathrm{cavity}}}}\,\Delta r_{\mathrm{cavity}} \ . \tag{18}$$

based on the flux conservation. For instance, in the 170 GHz gyrotron 0.5 mm offset of the beam in the cavity results in more than 1 cm offset at the end of collector. This will cause difficulties for the conventional MDC concept, which has to use low magnetic field in order to perform well; whereas for this $\boldsymbol{E}\times\boldsymbol{B}$ concept there is no problem at all, as shown in Fig. 16. Even a larger offset up to 0.8 mm would not cause any significant reduction of the performance.

V. CONCLUSIONS

The basic design of a feasible and promising gyrotron MDC is presented. In this design, a radial $\boldsymbol{E}\times\boldsymbol{B}$ drift is created by the azimuthal electric field and longitudinal magnetic field, where the electric field is sustained by a pair of helical electrodes. Utilizing the $\boldsymbol{E}\times\boldsymbol{B}$ drift,

this kind of MDC sorts electrons reliably, hence it has the potential to achieve very high collector efficiency. An example of a two-stage collector for the EU 170 GHz, 1 MW ITER gyrotron was simulated using a realistic spent electron beam. This two-stage collector is able to raise the gyrotron overall efficiency from 50 % to more than 60 %. The efficiency reduction by secondary electrons (including the elastically and inelastically reflected ones) is insignificant, due to the facts that firstly, the secondary electrons also experience the same $\boldsymbol{E}\times\boldsymbol{B}$ drift like the primary ones and are guided back to the first electrode; secondly, there is in principle no local accelerating electric field which back streams the secondary electrons from the second stage.

The analysis of this concept is relatively simple compared to the other gyrotron MDC concepts. The shape and size of this kind of collector can be approximately modeled without numerical calculations. Both trajectory-tracking and particle-in-cell solvers built in CST Particle Studio are used to verify the design. Their convergences are presented and the results of both methods are in close agreement.

Tolerance studies shows that this MDC design is resilience to the beam current and misalignment of the electron beam as well as reasonable external perturbation magnetic fields from tokamak and neighboring gyrotrons.

However, there is a straight slot joining the ends of the helical electrodes together. It simply separates the collector stages, but introduces an undesired drift towards the center axis. A small part of low energetic electrons can be reflected due to this drift. In this specific design example, 1.5 % of the beam current is reflected. Even though the ratio of reflected current can be further reduced via parameter optimizations, there shall be improved designs, which can fundamentally minimize or even avoid the back streaming current. Such improved designs will be discussed in Part II of this work.

To further extend this basic design, the MDC could have more stages by introducing more helical electrodes. Instead of a helix curling 360°, there could be two or more helices dividing the azimuthal circle into sectors, to shrink the MDC size. Also the torsion of the helix can be optimized rather than using a constant value to achieve a uniform drift strength on any longitudinal position, so that the collector may be further optimized.

ACKNOWLEDGMENTS

This work has been carried out within the framework of the EUROfusion Consortium and has received funding from the Euratom research and training program 2014–2018 under grant agreement No. 633053. The views and opinions expressed herein do not necessarily reflect those of the European Commission.

REFERENCES

[1]J. Jelonnek, S. Alberti, K. Avramidis, V. Erckmann, G. Gantenbein, K. Hesch, J.-P. Hogge, S. Illy, J. Jin, S. Kern, I. Pagonakis, B. Piosczyk, T. Rzesnicki, A. Samartsev, and M. Thumm, Fusion Science and Technology **64**, 505 (2013).

[2]K. Sakamoto, M. Tsuneoka, A. Kasugai, T. Imai, T. Kariya, K. Hayashi, and Y. Mitsunaka, Physical review letters **73**, 3532 (1994).

[3]B. Piosczyk, C. T. Iatrou, G. Dammertz, and M. Thumm, IEEE Trans. Plasma Sci. **24**, 579 (1996).

[4]M. Y. Glyavin, A. Kuftin, N. Venediktov, and V. Zapevalov, International journal of infrared and millimeter waves **18**, 2129 (1997).

[5]C. Wu, I. Pagonakis, S. Illy, M. Thumm, G. Gantenbein, and J. Jelonnek, in *German Microwave Conference (GeMiC)* (2016) pp. 365–368.

[6]T. Okoshi, E.-B. Chiu, and S. Matsuki, IEEE Trans. Electron Devices **19**, 104 (1972).

[7]H. G. Kosmahl, IEEE Proceedings **70**, 1325 (1982).

[8]A. Singh, S. Rajapatirana, Y. Men, V. Granatstein, R. Ives, and A. Antolak, IEEE Trans. Plasma Sci. **27**, 490 (1999).

[9]G. Ling, B. Piosczyk, and M. K. Thumm, IEEE Trans. Plasma Sci. **28**, 606 (2000).

[10]M. Y. Glyavin, M. V. Morozkin, and M. I. Petelin, Radiophysics and quantum electronics **49**, 811 (2006).

[11]I. G. Pagonakis, J. P. Hogge, S. Alberti, K. A. Avramides, and J. L. Vomvoridis, IEEE Trans. Plasma Sci. **36**, 469 (2008).

[12]I. G. Pagonakis, C. Wu, K. A. Avramidis, G. Gantenbein, S. Illy, M. Thumm, and J. Jelonnek, in *Proc. 42th Int. Conf. Infrared, Millimeter and Terahertz waves (IRMMW-THz)* (2017).

[13]I. G. Pagonakis, C. Wu, S. Illy, and J. Jelonnek, Physics of Plasmas **23**, 043114 (2016).

[14]C. Wu, I. G. Pagonakis, G. Gantenbein, S. Illy, M. Thumm, and J. Jelonnek, Physics of Plasmas **24**, 043102 (2017).

[15]C. Wu, I. G. Pagonakis, S. Illy, G. Gantenbein, M. Thumm, and J. Jelonnek, in *2017 IEEE International Vacuum Electronics Conference* (2017) pp. 1–2.

[16]O. I. Louksha and P. A. Trofimov, Technical Physics Letters **41**, 884 (2015).

[17]A. Malygin, S. Illy, I. G. Pagonakis, B. Piosczyk, S. Kern, J. Weggen, M. Thumm, J. Jelonnek, K. A. Avramides, R. L. Ives, D. Marsden, and G. Collins, IEEE Trans. Plasma Sci. **41**, 2717 (2013).

[18]L. Zhang, W. He, A. W. Cross, A. D. R. Phelps, K. Ronald, and C. G. Whyte, IEEE Trans. Plasma Sci. **37**, 2328 (2009).

[19]I. G. Pagonakis, F. Li, S. Illy, B. Piosczyk, S. Alberti, J.-P. Hogge, S. Kern, M. Henderson, and C. Darbos, IEEE Trans. Plasma Sci. **40**, 1945 (2012).

[20]B. Ell, I. G. Pagonakis, G. Gantenbein, S. Illy, M. Thumm, and J. Jelonnek, IEEE Trans. Electron Devices **64**, 3421 (2017).

[21]A. Samartsev, G. Dammertz, G. Gantenbein, J. Jelonnek, S. Illy, and M. Thumm, IEEE Trans. Plasma Sci. **41**, 872 (2013).